Nuclear Lattice Effective Field Theory: Status A.D. 2024

Ulf-G. Meißner[1,2,3]

[1] Helmholtz-Institut für Strahlen- und Kernphysik and Bethe Center for Theoretical Physics, Universität Bonn, D-53115 Bonn, Germany
E-mail: meissner@hiskp.uni-bonn.de

[2] Institute for Advanced Simulation (IAS-4). Forschungszentrum Jülich, 52425 Jülich, Germany

I discuss recent developments in nuclear lattice effective field theory, which is a premier tool in the theory of nuclear structure and reactions. Topics include the wavefunction matching method as a new tool for quantum many-body theory, allowing for accurate calculations at N3LO in the chiral expansion, as well as applications of the precise forces in few- and many nucleon systems. I also discuss a first step for precision hypernuclear physics, describe the solution of a puzzle related to the ^{4}He monopole transition form factor, discuss the calculation of hyper-neutron matter and give new insights how Big Bang nucleosynthesis constrains fundamental parameters of the Standard Model.

1 Introduction

Understanding the formation of strongly interacting systems such a atomic nuclei from first principles calculations is still one of the biggest challenges within contemporary theoretical physics. While the theory of the strong interactions, Quantum Chromodynamics (QCD), is well tested in many processes, the matter that leads to life in our Universe is based on nuclei, which are self-bound systems of nucleons (protons and neutrons). As the nucleons themselves consist of quarks and gluons, and hence are not fundamental degrees of freedom, the forces between nucleons are not completely given in terms of two-body interactions, but include three-body and higher order interaction terms. Much progress in the understanding of the structure and dynamics of nuclei has been made in the context of Nuclear Lattice Effective Field Theory (NLEFT)[1], which combines the so successful low-energy chiral effective field theory of QCD with stochastic methods (Monte Carlo simulations). While direct calculations of nuclei based on quarks and gluons in the framework of lattice QCD are essentially impossible due to the severe sign problem, formulating the nuclear forces in terms of protons, neutrons and pions is not only more appropriate, but also comes with the added value of the approximate Wigner SU(4) (spin-isospin) symmetry of the underlying nuclear interactions. This symmetry in fact suppresses the sign oscillations strongly, and in the limit of an exact Wigner SU(4) symmetry, spin-isospin saturated nuclei like e.g. ^{4}He are free of any sign oscillation. In NLEFT simulations, Euclidean space-time is discretized on a torus of volume $L^3 \times L_t$, where L is the side length of the spatial dimension, and L_t denotes the extent of the Euclidean time dimension. The lattice spacing in the spatial (temporal) dimensions is a (a_t). The maximal momentum on the lattice is $p_{\rm max} \equiv \pi/a$, which serves as the UV regulator of the theory. Nucleons are point-like particles on the lattice sites, and the interactions between nucleons (pion exchanges and contact terms) are treated as insertions on the nucleon world lines via auxiliary-field representations. Properties of multi-nucleon systems are computed by means of the projection Monte Carlo (MC) method. Each nucleon is treated as a single particle propagating in a

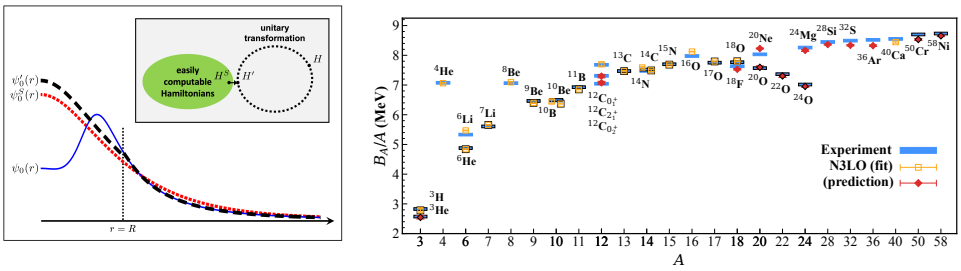

Figure 1. Left panel: Pictoral representation of wavefunction matching. The simple Hamiltonian H^S is an easily computable Hamiltonian while the high-fidelity Hamiltonian H is not. A unitary transformation on the two-nucleon interaction with finite range R is used to produce a new Hamiltonian H' that is close to H^S. In each two-body channel, the ground state wave function of H' matches the ground state wave function of H for $r > R$ and is proportional to the ground state wave function of H^S for $r < R$. Right panel: Results for nuclear binding energies using wave function matching. Calculated ground state and excited state energies of some selected nuclei with up to $A = 58$ at N3LO in chiral EFT and comparison with experimental data. The nuclei used in the fit of the higher-order three-nucleon interactions are labelled with open squares, while the other nuclei are predictions denoted with filled diamonds.

fluctuating background of pion and auxiliary fields. Both local and non-local smearings are applied to the nucleon creation and annihilation operators. Euclidean time projection is started from some initial state Ψ_A for Z protons and N neutrons (with $A = Z + N$). One calculates the ground state energy and other properties from the correlation function $Z(t) \equiv \langle \Psi_A | \exp(-tH) | \Psi_A \rangle = \mathrm{Tr}\{M^{L_t}\}$, in the limit of large Euclidean projection time t, with M the normal-ordered transfer-matrix operator and L_t the number of Euclidean time steps. Higher-order contributions are computed as perturbative corrections to the LO results. A much more detailed description is given in the monograph[1].

2 Wavefunction matching

Quantum Monte Carlo (QMC) simulations are a powerful and efficient method that can describe strong correlations in quantum many-body systems. No assumptions about the nature of the system are necessary, and the computational effort grows only as a low power of the number of particles. For many problems of interest, a simple Hamiltonian H^S can be found that describes the energies and other observables of the many-body system in fair agreement with empirical data and is easily computable using MC methods. On the other hand, realistic high-fidelity Hamiltonians usually suffer from severe sign problems with positive and negative contributions to the averages cancelling each other, so that Monte Carlo calculations become impractical. In Ref.[2], this problem was solved introducing a new approach called wavefunction matching (WFM). While keeping the observable physics unchanged, wave functionmatching creates a new high-fidelity Hamiltonian H' such that wave functions at short distances match that of a simple Hamiltonian H^S which is easily computed. This allows for a rapidly converging expansion in powers of the difference $H' - H^S$. WFM can be used with any computational scheme. In the following analysis, we focus on the case of QMC simulations, where the method presents a promising and practical strategy for evading the sign problem in realistic calculations of nuclear quantum many-body systems. The basic idea of WFM is easily described. Starting from a

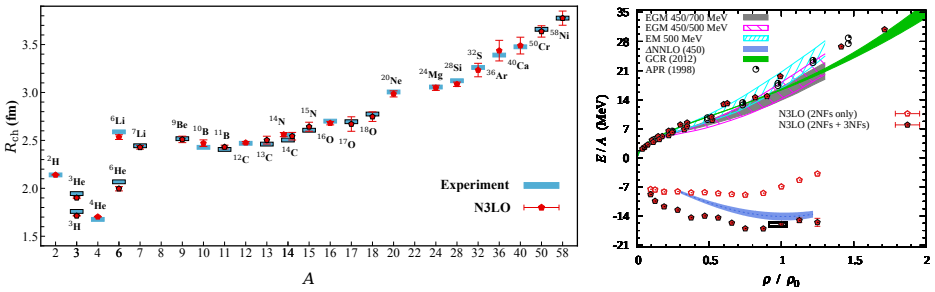

Figure 2. Left panel: Predictions for charge radii of nuclei up to $A = 58$ at N3LO in chiral EFT in comparison to the experimental data. Right panel: Predictions for pure neutron matter energy per neutron and symmetric nuclear matter energy per nucleon as a function of density at N3LO in chiral EFT. For comparison we show the results Refs.[5–8]. The empirical saturation point is labeled with a black rectangular box.

realistic high-fidelity Hamiltonian H, WFM defines a new Hamiltonian

$$H' = U^\dagger H U \ , \tag{1}$$

where U is a unitary tansformation and $U^\dagger$ its Hermitian conjugate. More precsiely, we consider the two-nucleon interaction here. In each two-body angular momentum channel, the unitary transformation U is active only when the separation distance between two particles is less than some chosen distance R. Let us write $\psi_0(r)$, $\psi_0'(r)$, and $\psi_0^S(r)$ for the ground state wave functions of H, H', and the simple Hamiltonian H^S, respectively. The transformation U is defined such that $\psi_0'(r)$ is proportional to $\psi_0^S(r)$ for $r < R$. The simple Hamiltonian is chosen so that the constant of proportionality is close to 1. For $r > R$, however, U is not active and so $\psi_0'(r)$ remains equal $\psi_0(r)$. This is illustrated in the left panel of Fig. 1. In the NLEFT application discussed here, the simple Hamiltonian consists of SU(4) invariant two-body forces as well as regularized one-pion exchange. All higher order corrections are treated in first order perturbation theory. The short-distance parts of the chiral three-nucleon (3N) interactions are then tuned to minimize errors in the binding energies of selected light and medium-mass nuclei. A total of six additional 3N parameters are adjusted, and it is found that with just one parameter, the root-mean-square-deviation (RMSD) for the energy per nucleon drops from 1.2 MeV down to 0.4 MeV. With the addition of a few additional parameters, the RMSD per nucleon drops further to about 0.1 MeV, as shown in the right panel of Fig. 1. Having fixed all parameters, we can now make predictions. In the left panel of Fig. 2, the results for the charge radii of nuclei with up to $A = 58$ nucleons are shown. No charge radii data were used to fit any interaction parameters. The one-standard-deviation point estimate error bars represent computational uncertainties due to MC errors, infinite volume extrapolation, and infinite time extrapolation. The agreement with empirical results is quite good, with an RMSD of about 0.03 fm. Note that the larger errors for the heaviest nuclei are statistical and can be decreased by utilizing greater computational resources. This solves the long-standing "radius puzzle" observed in all continuum *ab initio* many-body calculations, namely that when getting the correct binding energies, the nuclear radii come out too small, see e.g. Refs.[3,4]. In the right panel of Fig. 2, lattice results for the energy per nucleon versus density for pure neutron matter and symmetric nuclear matter are shown. None of the neutron matter and symmetric nuclear matter data were used to fit any interaction parameters. The density is expressed as a fraction of the saturation density for nuclear matter, $\rho_0 = 0.17$ fm^{-3}. For the neutron

matter calculations, we consider 14 to 80 neutrons in periodic box lengths ranging from 6.58 fm to 13.2 fm. For the symmetric nuclear matter calculations, we use system sizes from 12 to 160 nucleons in a periodic box of length 9.21 fm. We see that the neutron matter calculations agree well with previous calculations. Within the uncertainties due to finite system size corrections, the symmetric nuclear matter calculations show saturation at an energy and density consistent with the empirical saturation point labeled with the black rectangular box. The relative uncertainties due to finite system size are at the 10% level for the energy.

3 Testing the high-fidelity interactions

Next, the so determined N3LO high-fidelity interactions are tested in a number of calculations, which we discuss briefly.

3.1 Structure factors for hot neutron matter

In Ref.[9] the first *ab initio* lattice calculation of spin and density correlations in hot neutron matter using the high-fidelity interactions at N3LO in chiral EFT was done. These correlations have a large impact on neutrino heating and shock revival in core-collapse supernovae and are encapsulated in functions called structure factors. Unfortunately, calculations of structure factors using high-fidelity chiral interactions were well out of reach using existing computational methods. To solve the problem, a computational approach called the rank-one operator (RO) method is introduced. The RO method is a general technique with broad applications to simulations of fermionic many-body systems. It solves the problem of exponential scaling of computational effort when using perturbation theory for higher-body operators and higher-order corrections. Using the RO method, we compute the vector and axial static structure factors for hot neutron matter as a function of temperature and density given by:

$$\begin{aligned} S_{\rm v}(\boldsymbol{q}) &= \frac{1}{L^3}\sum_{\boldsymbol{n}\boldsymbol{n}'} \mathrm{e}^{-i\boldsymbol{q}\cdot\boldsymbol{n}} \left[\langle\hat{\rho}(\boldsymbol{n}+\boldsymbol{n}')\hat{\rho}(\boldsymbol{n}')\rangle - (\rho^0)^2\right], \\ S_{\rm a}(\boldsymbol{q}) &= \frac{1}{L^3}\sum_{\boldsymbol{n}\boldsymbol{n}'} \mathrm{e}^{-i\boldsymbol{q}\cdot\boldsymbol{n}} \left[\langle\hat{\rho}_z(\boldsymbol{n}+\boldsymbol{n}')\hat{\rho}_z(\boldsymbol{n}')\rangle - (\rho_z^0)^2\right], \end{aligned} \tag{2}$$

where $\hat{\rho}$ and $\hat{\rho}_z$ are the density and the spin-density operators, respectively, and $\boldsymbol{n}, \boldsymbol{n}'$ represent coordinates on the L^3 cubic lattice. The *ab initio* lattice results are in good agreement with virial expansion calculations at low densities but are more reliable at higher densities, see the left panel of Fig. 3. Random phase approximation codes used to estimate neutrino opacity in core-collapse supernovae simulations can now be calibrated with these precise *ab initio* lattice calculations.

3.2 Nuclear charge radii of silicon isotopes

The next test of the N3LO forces was done in collaboration with experimentalists from FRIB[10]. They determined the nuclear charge radius of ^{32}Si using collinear laser spectroscopy, leading to $R_{\rm ch}(^{32}\mathrm{Si}) = 3.153(12)\,\mathrm{fm}$. The experimental result was confronted

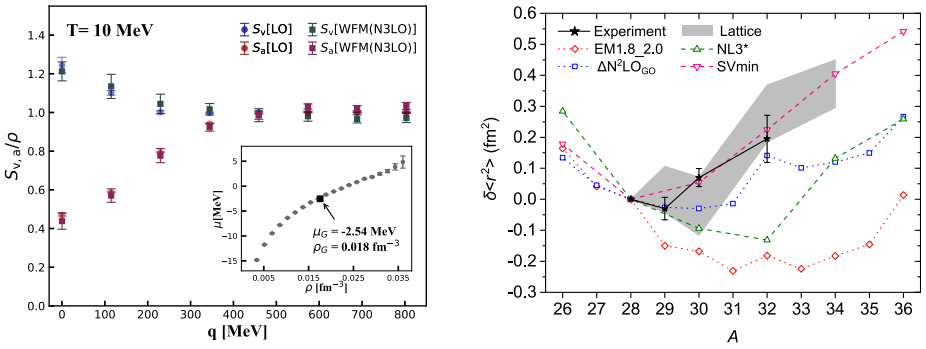

Figure 3. Left panel: Calculated momentum dependent neutron matter structure factors $S_{\rm v}$ and $S_{\rm a}$ at $T = 10$ MeV. WFM(N3LO) represents the NLEFT calculations with the WFM N3LO interaction. The insert figure shows calculated chemical potentials of canonical ensemble systems which are used for the construction of grand canonial ensemble at the chemical potential $\mu_G = -2.54$ MeV and the density $\rho_G = 0.01758(4)$ fm^{-3}. Right panel: Experimental and theoretical differential mean square charge radii of Si. The NLEFT calculation provided an uncertainty which is plotted as the gray band.

with *ab initio* NLEFT, valence-space in-medium similarity renormalization group, and mean field calculations, highlighting important achievements and challenges of modern many-body methods. The lattice simulations for the charge radii are new calculations based upon the N3LO chiral interactions described in Ref.[2] with two additional improvements made. Rather than a global fit to all nuclei, we fit the three-nucleon coefficients $c_E^{(l)}$ and $c_E^{(t)}$ to ensure good agreement with the binding energies of the silicon isotopic chain. We also use the rank-one operator method introduced in Ref.[9] to compute the charge radii. As shown in the right panel of Fig. 3, the NLEFT results are in good agreement with the measured charge radii along the Si isotope chain from $A = 28$ to $A = 32$. The charge radius of ^{32}Si completes the radii of the mirror pair ^{32}Ar - ^{32}Si, whose difference is correlated to the slope L of the symmetry energy in the nuclear equation of state. The NLEFT result for L was determined from the calculations of pure neutron matter in Ref.[2], giving $L = 55(7)$ MeV, which agrees with complementary observables.

3.3 The triton lifetime

Nuclear β and double-β decays are fine probes of the weak interactions in their interplay with the strong force. Arguably the best example is the extraction of the CKM matrix element V_{ud} from superallowed β decays[11]. Triton β-decay is the process where ^{3}H decays into ^{3}He, an electron, and an electron antineutrino, $^3\mathrm{H} \to {}^3\mathrm{He} + e^- + \bar{\nu}_e$. The matrix elements of the weak transition are crucial to understanding this decay process. Thus, this decay serves as a benchmark for calculating weak nuclear decays. In addition, it is known that triton β-decay, that is the triton lifetime, together with the binding energies in the $A = 3$ system can lead to a robust determination of the low-energy constants c_D and c_E parameterizing the leading three-nucleon forces in chiral EFT[12]. The triton lifetime is given in terms of two matrix elements (MEs), refered to as the Fermi and the Gamov-Teller

MEs,

$$\langle F\rangle = \sum_{n=1}^{3}\langle {}^3\mathrm{He}\|\tau_{n,+}\|{}^3\mathrm{H}\rangle \ , \quad \langle GT\rangle = \sum_{n=1}^{3}\langle {}^3\mathrm{He}||\sigma_n\tau_{n,+}||{}^3\mathrm{H}\rangle \ , \tag{3}$$

in order. Here, $\tau_{n,+}$ is the isospin-raising operator and the σ_n are the nucleon spin matrices. Despite the success of the WFM method in improving theoretical precision, the calculations in Ref.[2] were carried out using first-order perturbation theory. Since first-order perturbation theory only provides corrections to the energy and not to the wavefunctions, triton β-decay calculations at N3LO, requiring higher-order perturbative corrections for realistic wave functions, cannot be directly performed using the methods from Ref.[2]. One potential solution to this challenge is to extend the calculations to second-order perturbation theory. Recent advances in perturbative QMC methods, as detailed in Ref.[13], provide an effective framework for incorporating higher-order perturbative corrections, making it particularly well-suited for applications to heavier nuclei. Alternatively, fully non-perturbative methods can be applied to light nuclear systems to generate realistic wave functions at N3LO, as required for triton β-decay calculation. This was done in Ref.[14]. Performing this non-perturbative calculation, the Fermi ME as well as the Gamow-Teller ME are simultaneously obtained,

$$\langle F\rangle = 0.99949(11) \ , \quad \langle GT\rangle = 1.6743(58) \ , \tag{4}$$

where the uncertainty stems from the large L_t extrapolation and the variation of the strengths of the the one-pion exchange and contact term topologies of the three-nucleon forces. These results are consistent with earlier theoretical calculations, confirming the robustness of our approach. The corresponding lifetime is given by $(1+\delta_R)\,t_{1/2}\,f_V = 1105.1(74)$ s, consistent with the empirical determinations, $(1+\delta_R)\,t_{1/2}\,f_V = 1132.1(25)\,\mathrm{s}$. The remaining discrepancies are due to the fact that the corrections to the pion exchange currents have not yet been included. This study marks a significant advancement in the systematic application of NLEFT to nuclear β-decay processes, paving the way for future high-precision calculations in more complex nuclear systems, such as neutrinoless double-β decay in ^{48}Ca or ^{76}Ge.

4 Towards Hypernuclei from NLEFT

Understanding the strong interactions in the light quark sector is crucial for a comprehensive description of baryonic systems such as nuclei and hypernuclei. The study of hypernuclei provides valuable insights into the baryon-baryon interactions, and an accurate description of the properties of hypernuclei requires a systematic formulation of interactions between hyperons and nucleons, as well as constraining their low-energy constants (LECs). The great success of both phenomenological potential models and chiral EFT for nucleons is based on rich and precise NN-scattering data and nuclear binding energies. However, due to the scarcity of hyperon-nucleon and hyperon-hyperon scattering data, the spectra of hypernuclei are pivotal in constraining the hyperon-nucleon and hyperon-hyperon interactions, deepening our understanding of SU(3) flavor symmetry breaking and charge symmetry breaking in strong interactions. In Ref.[15] we calculated the ground state and

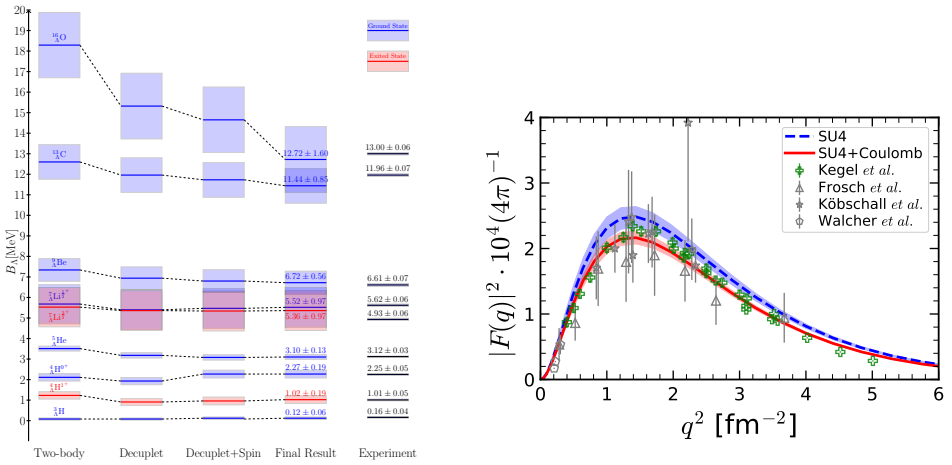

Figure 4. Left panel: Λ separation energies for different YNN forces (decuplet saturation: $C_1 = C_3$ and $C_2 = 0$, decuplet plus spin: $C_1 = C_3$ and $C_2 \neq 0$, final result: $C_1 \neq C_2 \neq C_3 \neq 0$). The large improvement resulting from the introduction of the spin-dependent three-body force $\sim C_2$ is clearly visible. The experimental values are taken from Ref.[16], where we averaged the four-body systems. Ground states are depicted in blue, excited states in red. The uncertainties are indicated by the shaded areas. Right panel: Calculated monople form factor of the $0_2^+ \to 0_1^+$ transition in ^{4}He compared to the recent data from Mainz[18] (green squares) and the older data (grey symbols). Blue dashed line: SU(4) symmetric strong interaction with all parameters determined in Ref.[20]. Red solid line: adding the Coulomb interaction perturbatively. The uncertainty bands in the lattice results include stochastic errors and uncertainties in the Euclidean time extrapolation

excited state energies of hypernuclei up to $A = 16$. Our calculations employ the high-fidelity chiral interactions at N3LO for nucleons from Ref. [2] and the leading-order S-wave hyperon-nucleon (YN) interactions are given by

$$V_{\rm YN} = \frac{1}{4} C_{YN}^S (\mathbb{1} - \boldsymbol{\sigma_1} \cdot \boldsymbol{\sigma_2}) + \frac{1}{4} C_{YN}^T (3 + \boldsymbol{\sigma_1} \cdot \boldsymbol{\sigma_2}) \,. \tag{5}$$

The LECs $C_{YN}^{S,T}$ are determined by a fit to the unpolarized $\Lambda p \to \Lambda p$ cross section and the hypertriton binding energy. The hyperon-nucleon-nucleon (YNN) interactions are given by

$$\begin{aligned} V_{\rm YNN} = {} & C_1 (\mathbb{1} - \boldsymbol{\sigma}_2 \cdot \boldsymbol{\sigma}_3)(3 + \boldsymbol{\tau}_2 \cdot \boldsymbol{\tau}_3) + C_2 \, \boldsymbol{\sigma}_1 \cdot (\boldsymbol{\sigma}_2 + \boldsymbol{\sigma}_3)(\mathbb{1} - \boldsymbol{\tau}_2 \cdot \boldsymbol{\tau}_3) \\ & + C_3 (3 + \boldsymbol{\sigma}_2 \cdot \boldsymbol{\sigma}_3)(\mathbb{1} - \boldsymbol{\tau}_2 \cdot \boldsymbol{\tau}_3) \,, \end{aligned} \tag{6}$$

and the LECs $C_{1,2,3}$ are determined by hypernuclear systems with $A = 4$ and 5. For the YNN interactions, we consider all possible forms of short-distance smearing. In our analysis, we calculate the RMSD over all calculated hypernuclear separation energies with $A \geq 4$, which are used to assess the accuracy of the YNN interactions in describing hypernuclei. In the left panel of Fig. 4 we show results for hypernuclei from $^3_\Lambda$He to $^{16}_\Lambda$O, where the hypernuclei with $A \leq 5$ shown here are included in the fit, while the other hypernuclei are predictions. We find that, within stochastic uncertainties of the MC simulations, our Hamiltonian can accurately describe hypernuclear systems. Clearly, improvements in the considered interactions here should be perforemd. We recommend including pion exchange forces in both the two-body and three-body sector. These forces not only allow

for an automatic inclusion of higher momentum contributions but also make excited states available in typical multichannel calculations, Additionally, this approach enables the inclusion of higher orders in the chiral expansion, which are necessary for better phase shift descriptions at higher orders that will also improve the description of the hypernuclei.

5 The puzzling ^{4}He transition form factor

The ^{4}He nucleus, the α-particle, is considered to be a benchmark nucleus for our understanding of the nuclear forces and the few-body methods to solve the nuclear A-body problem[17]. The attractive nucleon-nucleon interaction makes this highly symmetric four-nucleon system enormously stable. Furthermore, its first excited state has the same quantum numbers as the ground state, $J^P = 0^+$ with $J(P)$ the spin (parity), but is located about 20 MeV above the ground state. This large energy of the first quantum excitation makes the system difficult to perturb. This isoscalar monopole resonance of the ^{4}He nucleus presents a challenge to our understanding of nuclear few-body systems and the underlying nuclear forces. The recent precision measurement of the corresponding transition form factor of the first excited state to the ground state at the Mainz Microtrom MAMI[18] compared with *ab initio* calculations based on the Lorentz-integral transformation method using phenomenological potentials as well as potentials based on chiral EFT revealed sizeable discrepancies as shown in Fig. 3 of Ref.[18]. We addressed this issue in Ref.[19] within the framework of the minimal nuclear interaction that reproduces the ground state properties of light nuclei, medium-mass nuclei, and neutron matter simultaneously with no more than a few percent error in the energies and charge radii[20,21]. The transition form factor $F(q)$ of the monopole transition is related to the transition density $\rho_{\rm tr}(r)$ by

$$F(q) = \frac{4\pi}{Z}\int_0^\infty \rho_{\rm tr}(r) j_0(qr) r^2 dr = \frac{1}{Z}\sum_{\lambda=1}^{\infty} \frac{(-1)^\lambda}{(2\lambda+1)!} q^{2\lambda} \langle r^{2\lambda}\rangle_{\rm tr} \,, \tag{7}$$

with Z the charge of the nucleus under consideration. Here $Z = 2$, and $\rho_{\rm tr}(r) = \langle 0_1^+|\hat{\rho}(\vec{r})|0_2^+\rangle$ is the matrix element of the charge density operator $\hat{\rho}(\vec{r})$ between the ground state 0_1^+ and the first excited 0_2^+ state. We also display the expansion in moments in Eq. (7). The first excited state of ^{4}He is a resonance that sits just above the ^{3}H+p threshold. In order to study this continuum state, we perform calculations using three different cubic periodic boxes with lengths $L = 10, 11, 12$ in lattice units, corresponding to $L = 13.2$ fm, 14.5 fm, 15.7 fm. The corresponding ground and first excited state energies are $E(0_1^+) = -28.30(3)$ MeV and $E(0_2^+) = -7.96(9)$ MeV that compare well with the experimental values of -28.30 MeV and -8.09 MeV, repsectively. Next, we turn to the analysis of the transition form factor, denoted as $F(q)$. In the framework of NLEFT, observables such as nucleon density distributions, charge radii and form factors can be computed using the pinhole algorithm. First, we consider the SU(4)-symmetric interactions without Coulomb. The resulting form factor is depicted by the blue dashed line in the right panel of Fig. 4. It somewhat overshoots the data, although the error band associated with stochastic errors and the large L_t extrpolation almost encompasses the data. Including the Coulomb interaction leads to an overall reduction of the transition form factor as shown by the red solid line in the right panel of Fig. 4. Overall, we achieve a good reproduction of the data and the uncertainty band is also somewhat reduced. This is due to the fact that

inclusion of the Coulomb interaction leads to smaller fluctuations in the Monte Carlo data when extrapolating to large L_t. Consequently, we find that the nuclear interaction defined in Ref.[20], which has already been shown to reproduce the essential elements of nuclear binding, also leads to a good description of the α-particle transition $0_2^+ \to 0_1^+$ form factor without adjusting any parameters. Thus, the nuclear forces relevant to this system are under good control, and we do not find the puzzle mentioned in Ref.[18], see also Refs.[22,23].

6 *Ab initio* calculation of hyper-neutron matter

The equation of state (EoS) of neutron matter plays a decisive role to understand the neutron star properties and the gravitational waves from neutron star mergers. At sufficient densities, the appearance of hyperons generally softens the EoS, leading to a reduction in the maximum mass of neutron stars well below the observed values of about 2 solar masses. Even though repulsive three-body forces are known to solve this so-called "hyperon puzzle", see e.g. Refs.[24,25], so far performing *ab initio* MC calculations with a substantial number of hyperons has remained elusive. We addressed this challenge by employing NLEFT in Ref.[26]. First, we had to develop an algorithm that allows to go to densities beyond twice nuclear matter densities reached so far in QMC simulations which is not sufficient for the description of neutron stars. To achieve that, we combine the smeared nucleon operator with the operator representing the Λ hyperon, as detailed in Ref.[26]. This enables simulations of systems consisting of both arbitrary number of nucleons and arbitrary number of Λ hyperons with a single auxiliary field. Second, we work with smeared concact interactions only, which allows to include all possible interactions, that is NN, NY, YY, NNN, NNY and NYY, which was never done in a QMC simulations before. The NN and NNN LECs are determined from a combined fit to the S-wave phase shifts and the saturation properties of nuclear matter, with $\rho_0 = 0.17\,\mathrm{fm}^{-3}$ the nuclear matter density. This calculation generates a very stiff neutron matter EoS as shown in the left panel of Fig. 5, and it required required up to 232 nucleons in the finite volume to achieve densities of $5\rho_0$ as in the interior of neutron stars. Next, we show three different EoS when hyperons are included. The NNΛ and N$\Lambda\Lambda$ forces are constrained by the separation energies of single- and double-Λ hypernuclei, spanning systems from ${}^{5}_{\Lambda}$He to ${}^{6}_{\Lambda\Lambda}$Be, denoted as HNM(I). It is difficult to probe the behavior of the EoS at high densities encountered in neutron stars in terrestrial laboratories, and various phenomenological schemes and microscopical models suggest that hyperons emerge in the inner core of neutron stars at densities around $\rho \approx (2-3)\rho_0$. Similar to using the saturation properties of symmetric nuclear matter to pin down the three-nucleon forces, we determined the NNΛ and N$\Lambda\Lambda$ forces by using the separation energies of hypernuclei and the Λ threshold densities $\rho_\Lambda^{\mathrm{th}}$ around $(2-3)\rho_0$ simultaneously in HNM(II) and HNM(III). We set $\rho_\Lambda^{\mathrm{th}}$ = 0.398(2)(5) fm^{-3} and 0.520(2)(6) fm^{-3} for HNM(II) and HNM(III), respectively. The corresponding EoSs are also shown in the left panel of Fig. 5. To fulfill the equilibrium condtion for the chemical potentials, $\mu_n = \mu_\Lambda$, we needed 102, 92, and 32 Λs for HNM(I), HMN(II) and HNM(III), in order. The EoS becomes stiffer at higher densities for these variants, indicating the inclusion of more repulsion in the three-body hyperon-nucleon interactions. As anticipated, the inclusion of hyperons results in a softer EoS and HNM(III) is the stiffest EoS when hyperons are included. The squared speed of sound, c_s^2, is also shown in the inset in the left panel of Fig. 5. It is observed that the causality limit ($c_s^2 < 1$) is fulfilled for both PNM and HNM. The EoS characterized

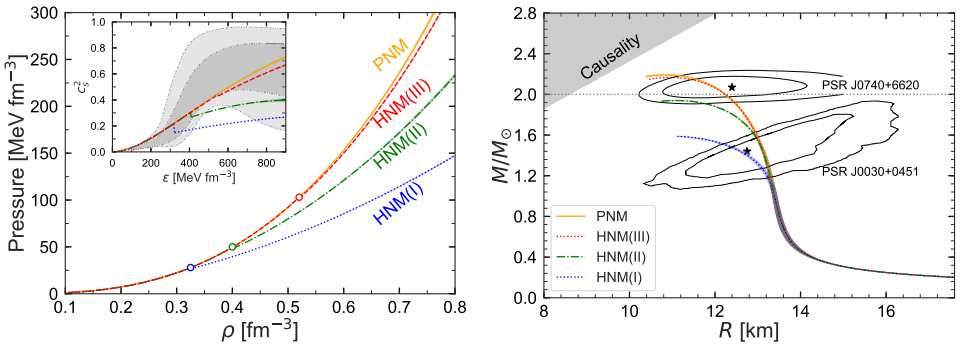

Figure 5. Left panel: EoS for PNM and HNM. The orange solid curve denotes pure neutron matter, obtained from the NN and NNN interactions. The red dashed line represents the EoS of HNM with hyperons interacting via the two-body interactions (NΛ and ΛΛ) and the third set of three-body hyperon-nucleon interaction (NNΛ and NΛΛ). The blue dotted curve and the green dot-dashed curve are calculated with the first and second sets of three-body hyperon-nucleon interactions. The Λ threshold densities $\rho_\Lambda^{\rm th}$ are marked by open circles. In the inset, the speed of sound corresponding to the PNM and HNM EOSs is shown. The gray shaded regions are the inference of the speed of sound for neutron star matter in view of the recent observational data[27]. Right panel: Neutron star mass-radius relation. The legend is the same as in the left panel. The gray horizontal dotted line represents $2M_\odot$. The inner and outer contours indicate the allowed area of mass and radius of neutron stars by NICER's analysis of PSR J0030+0451[30] and PSR J0740+6620[31]. The excluded causality region is also shown by the grey shaded region[32].

by nucleonic degrees of freedom exclusively demonstrate a monotonic increase in c_s^2 with increasing energy density. The appearances of Λ hyperons, however, induces changes in this behavior, leading to non-monotonic curves that signify the incorporation of additional degrees of freedom. The onset of Λ hyperons precipitates a sharp reduction in the speed of sound, marking a significant transition in the stiffness of the EoS. For comparison, the constraints on c_s^2 within the interiors of neutron stars inferred by a Bayesian inference method are also shown[27]. The "holy grail" of neutron-star structure, the mass-radius (MR) relation, is displayed in the right panel of Fig. 5. These relations for PNM and HNM are obtained by solving the Tolman-Oppenheimer-Volkoff (TOV) equations[28,29] with the EoSs of Fig. 5 (left panel). The appearance of Λ hyperons in neutron star matter remarkably reduces the predicted maximum mass compared to the PNM scenario. The maximum mass for PNM, HNM(I), HNM(II), and HNM(III) is 2.19(1)(1) $M_\odot$, 1.59(1)(1) $M_\odot$, 1.94(1)(1) $M_\odot$, and 2.17(1)(1) $M_\odot$, respectively. Note that three neutron stars have been measured to have gravitational masses close to $2M_\odot$ that significantly constrain the EoS of dense nuclear matter. Our results show that the inclusion of the NNΛ and NΛΛ interaction in HNM(III) leads to an EoS stiff enough such that the resulting neutron star maximum mass is compatible with the three mentioned measurements of neutron star masses. Therefore, the repulsion introduced by the hyperonic three-body interactions plays a crucial role, since it substantially increases the value of the Λ threshold density. Note that Ref.[26] also conatins the first *ab initio* calculation of the universal I-Love-Q relations, which connect the moment of inertia I, tidal deformability Λ, and the quadrupole moment Q in a slow rotation approximation. In the next steps, one should include the proton fraction, other hyperons of the baryon octet, and make use of the recently developed high-fidelity chiral interactions at N3LO [2], though this will pose a formidable computational challenge.

7 Big Bang nucleosynthesis as a probe of fundamental constants

Element generation in Big Bang nucleosynthesis (BBN) is a fine laboratory to study the possible variations of the fundamental parameters of the Standard Model, such as the quark masses or the electromagnetic fine-structure constant $\alpha_{\rm EM}$, see e.g. Ref.[33]. However, the reaction network is also very sensitive to the nuclear physics input, which so far has not been studied systematically. In Ref.[34] we investigated the dependence of primordial nuclear abundances on fundamental nuclear observables such as binding energies, scattering lengths, neutron lifetime, etc. by varying these quantities. The numerical computations were performed with four publicly available codes, thus facilitating an investigation of the model-dependent (systematic) uncertainties on these dependences. Indeed deviations of the order of a few percent are found. Moreover, accounting for the temperature dependence of the sensitivity of the rates to some relevant parameters leads to a reduction of the sensitivity of the final primordial abundances, which in some cases is appreciable. These effects are considered to be relevant for studies of the dependence of the nuclear abundances on fundamental parameters such as quark masses or couplings underlying the nuclear parameters studied here. Based on that work, we studied in Ref.[35] the dependence of the primordial nuclear abundances as a function of $\alpha_{\rm EM}$, keeping all other fundamental constants fixed. We updated the leading nuclear reaction rates, in particular the electromagnetic contribution to the neutron-proton mass difference pertinent to β-decays, and went beyond certain approximations made in the literature. In particular, we included the temperature-dependence of the leading nuclear reactions rates and assessed the systematic uncertainties by using four different publicly available codes for BBN. Disregarding the unsolved so-called lithium-problem, we find that the current values for the observationally based ^{2}H and ^{4}He abundances restrict the fractional change in $\alpha_{\rm EM}$ to less than 2% , which is a tighter bound than found in earlier works on the subject. Further, in Ref.[37], we presented an improved calculation of the light element abundances in the framework of BBN as a function of the Higgs vacuum expectation value v. We improved and corrected the recent calculation of Ref.[36] and earlier works on this topic by combining up-to-date lattice data on the nucleon mass, the axial-vector coupling, etc, with chiral EFT methods. The PDG result for the ^{4}He abundance can be explained within 2σ by $0.004 \leq \delta v/v \leq 0.007$. For deuterium we find the constraint $-0.0007 \leq \delta v/v \leq -0.0002$. These bounds are more stringent than what was found earlier, and, in partcular, the tightest bound is now set by dueterium, not ^{4}He any more (as in all earlier works). This is a significant step in the quest for finding the habitable universes as constrained by fundamental parameter variations in nuclear structure and reactions.

Acknowledgments

I thank my NLEFT colleagues for their contributions to the results presented here. The work reported here is part of the ERC AdG EXOTIC supported by the European Research Council (ERC) under the European Union's Horizon 2020 research and innovation programme (grant agreement No. 101018170). This work was also supported in part by the DFG (DFG Project ID 196253076 - TRR 110) through the funds provided to the Sino-German CRC 110 "Symmetries and the Emergence of Structure in QCD", by the Chinese Academy of Sciences (CAS) President's International Fellowship Initiative (PIFI)

(grant no. 2025PD0022), by the MKW NRW under the funding code NW21-024-A and by VolkswagenStiftung (grant no. 93562). The computational resources were provided by the Jülich Supercomputing Centre (JSC) at Forschungszentrum Jülich. Special resources on the JURECA-DC supercomputer at the JSC are particularly acknowledged.

References

1. T. A. Lähde and U.-G. Meißner, Lect. Notes Phys. **957** (2019), 1-396.
2. S. Elhatisari, *et al.*, Nature **630** (2024) no.8015, 59-63.
3. A. Cipollone, C. Barbieri and P. Navrátil, Phys. Rev. C **92** (2015) no.1, 014306.
4. P. Maris *et al.* [LENPIC], Phys. Rev. C **106** (2022) no.6, 064002.
5. A. Akmal, *et al.*, Phys. Rev. C **58** (1998), 1804-1828.
6. S. Gandolfi, J. Carlson and S. Reddy, Phys. Rev. C **85** (2012), 032801.
7. I. Tews, *et al.*, Phys. Rev. Lett. **110** (2013) no.3, 032504.
8. A. Ekström, *et al.*, Phys. Rev. C **97** (2018) no.2, 024332.
9. Y. Z. Ma, *et al.*, Phys. Rev. Lett. **132** (2024) no.23, 232502.
10. K. König, *et al.*, Phys. Rev. Lett. **132** (2024) no.16, 162502.
11. J. C. Hardy and I. S. Towner, Phys. Rev. C **91** (2015) no.2, 025501.
12. D. Gazit, *et al.*, Phys. Rev. Lett. **103** (2009), 102502.
13. B. N. Lu, *et al.*, Phys. Rev. Lett. **128** (2022) no.24, 242501.
14. S. Elhatisari, F. Hildenbrand and U.-G. Meißner, Phys. Lett. B **859** (2024) 139086.
15. F. Hildenbrand, S. Elhatisari, Z. Ren, U.-G. Meißner, Eur. Phys. J. A **60** (2024) 215.
16. P. Eckert, P. Achenbach and others, 2021, https://hypernuclei.kph.uni-mainz.de .
17. H. Kamada, *et al.*, Phys. Rev. C **64** (2001), 044001.
18. S. Kegel, *et al.*, Phys. Rev. Lett. **130** (2023) no.15, 152502.
19. U.-G. Meißner, *et al.*, Phys. Rev. Lett. **132** (2024) no.6, 062501.
20. B. N. Lu, *et al.*, Phys. Lett. B **797** (2019), 134863
21. S. Shen, *et al.*, Nature Commun. **14** (2023) no.1, 2777
22. N. Michel, *et al.*, Phys. Rev. Lett. **131** (2023) no.24, 242502.
23. M. Viviani, *et al.*, Few Body Syst. **65** (2024) no.3, 74.
24. J. Schaffner-Bielich, Nucl. Phys. A **804** (2008), 309-321.
25. D. Lonardoni, *et al.*, Phys. Rev. Lett. **114** (2015) no.9, 092301.
26. H. Tong, S. Elhatisari and U.-G. Meißner, [arXiv:2405.01887 [nucl-th]].
27. L. Brandes, W. Weise and N. Kaiser, Phys. Rev. D **108** (2023) no.9, 094014.
28. R. C. Tolman, Phys. Rev. **55** (1939), 364-373.
29. J. R. Oppenheimer and G. M. Volkoff, Phys. Rev. **55** (1939), 374-381.
30. M. C. Miller, *et al.*, Astrophys. J. Lett. **887** (2019) no.1, L24.
31. T. E. Riley, *et al.*, Astrophys. J. Lett. **918** (2021) no.2, L27.
32. J. M. Lattimer and M. Prakash, Phys. Rept. **442** (2007), 109-165.
33. F. C. Adams, Phys. Rept. **807** (2019), 1-111.
34. U.-G. Meißner and B. C. Metsch, Eur. Phys. J. A **58** (2022) no.11, 212.
35. U.-G. Meißner, B. C. Metsch and H. Meyer, Eur. Phys. J. A **59** (2023) no.10, 223.
36. A. K. Burns, *et al.*, Phys. Rev. D **109** (2024) no.12, 123506.
37. H. Meyer and U.-G. Meißner, JHEP **06** (2024), 074.